Competition between kinetics and thermodynamics during the growth of faceted crystal by phase field modeling

Marco Albani[*,1], Roberto Bergamaschini[1], Marco Salvalaglio[2], Axel Voigt[2,3], Leo Miglio[1], Francesco Montalenti[1]

[1] L-NESS and Dept. of Materials Science, Università di Milano - Bicocca, 20125, Milano, Italy,
[2] Institute of Scientific Computing, Technische Universität Dresden, 01062, Dresden, Germany
[3] Dresden Center for Computational Materials Science (DCMS), Technische Universität Dresden, 01062 Dresden, Germany

Key words: crystal faceting, incorporation time, kinetics, surface diffusion, phase-field

[*] Corresponding author: e-mail marco.albani@unimib.it

The faceting of a growing crystal is theoretically investigated by a continuum model including the incorporation kinetics of adatoms. This allows us for predictions beyond a simple Wulff analysis which typically refers to faceted morphologies in terms of the equilibrium crystal shape for crystals with an anisotropic surface-energy, or to steady-state kinetic shape when the crystals grow with orientation-dependent velocities. A phase-field approach is implemented in order to account simultaneously for these contributions in two- and three dimensions reproducing realistic kinetic pathways for the morphological evolution of crystal surfaces during growth. After a systematic characterization of the faceting determined by orientation-dependent incorporation times, several different crystal morphologies are found by tuning the relative weights of thermodynamic and kinetic driving forces. Applications to realistic systems are finally reported showing the versatility of the proposed approach and demonstrating the key role played by the incorporation dynamics in out-of-equilibrium growth processes.

1 Introduction Faceting is one of the most distinctive traits of a finite crystal, from the macroscopic scale down to the micro- and nanoscale [1]. In the latter case, the enhanced surface-to-volume ratio makes it a crucial aspect for material properties and applications. Understanding, and possibly controlling, the crystal faceting has then been the object of intensive studies dating back to the 19th century. Already in 1901, indeed, G. Wulff proposed its famous geometric construction [2] for predicting the equilibrium crystal shape (ECS) on the basis of the principle of surface energy minimization. This geometric procedure, formalized and demonstrated only decades later (see in particular Ref. [3]), is illustrated in Figure 1 in two dimensions (2D). Once the surface energy density γ is known as a function of the local surface orientation $\hat{\mathbf{n}}$, one traces its polar plot and at each point along it draws a plane normal to $\hat{\mathbf{n}}$. The inner envelope of all these planes corresponds to the ECS. This shape can be meant as the trade-off between the tendency toward exposing the facets having minimum energy and the minimization of the total surface area. The thermodynamic principles behind the definition of the ECS [4,5] find good applicability for inspecting the faceting of crystals under annealing or, more in general, in the case of close-to-equilibrium growth processes, i.e. at high temperature and slow growth rates. Indeed, adatoms at the surface must be sufficiently mobile to diffuse according to thermodynamic driving forces prior to their permanent incorporation in the crystal and/or being covered by additional deposited material.

When considering growth, out-of-equilibrium conditions can alter the crystal faceting corresponding to the ECS. A more convenient description of the crystal faceting during growth is then provided by the kinetic crystal shape (KCS), obtained by considering that each facet grows with

an assigned velocity $v = v(\hat{\mathbf{n}})$. The Wulff procedure can still be applied to determine the shape of the growing crystal just replacing γ with v [6–8], as in Figure 1.

Both the ECS and the KCS scale self-similarly with volume so that they just provide the final shape of the crystal, without any information on kinetic pathways. In particular, ECS describes the minimum energy configuration and the KCS provides a description of the growth front when stationary conditions hold. However, since normally the growth does not start from a crystal seed with the same shape of the KCS, a first transient state can be expected with changes in the relative extensions of facets, i.e. in contrast with the KCS. In a very simplified way, this evolution can be traced by evolving each point according to its velocity $v(\hat{\mathbf{n}})$ (Borgstrom construction [9]), as shown by the dashed profiles in the Figure 1(b). By simple geometric arguments, it can be shown that the slowest growing facets expand in size at the expenses of the fastest ones, up to expelling them from the growing profile if not present in the KCS[10].

While the ECS can be considered a property of the material for given environmental conditions e.g. temperature, (partial) pressure of the components, surface reconstruction, ..., and, in principle, it could be theoretically predicted by computing the surface energy of all possible facets, it is much more difficult to estimate the KCS without a direct comparison of experiments. Indeed, the growth rates of facets v result from a complex combination of surface/energetic properties and details of the growth procedure, e.g. kind of reactants, distribution of the species, chemical environment and possible side reactions (e.g. etching, passivation, ...), sticking/desorption at the surface, ... (for a topical review, see Ref. [1]). Reasonably, the set of possible facets should be the same for ECS and KCS but the two can be quite different and only a subset of such facets may really be distinguishable in a growing profile.

ECS and KCS can be considered the two limiting cases when the shape is defined by thermodynamics or by the growth kinetics, respectively. The former is established when the surface diffusion prevails over the deposition dynamics so that the material can redistribute to achieve the minimum energy configuration. Viceversa, the latter is obtained when only short-range diffusion is enabled so that the local velocity of the growth front is essentially determined by the net income of material.

An intermediate condition is yet possible if the timescale for adatom diffusion, before the incorporation in the crystal, becomes comparable with the one of deposition. This regime has been discussed in details by J.W. Cahn and J.E. Taylor in Ref. [11] (see also Ref. [12] for a detailed derivation) and takes into account that atoms deposited on the surface require a finite time to get incorporated in a definitive site during which they can migrate elsewhere. As this process is expected to significantly depend on the actual facets, it introduces another anisotropic contribution

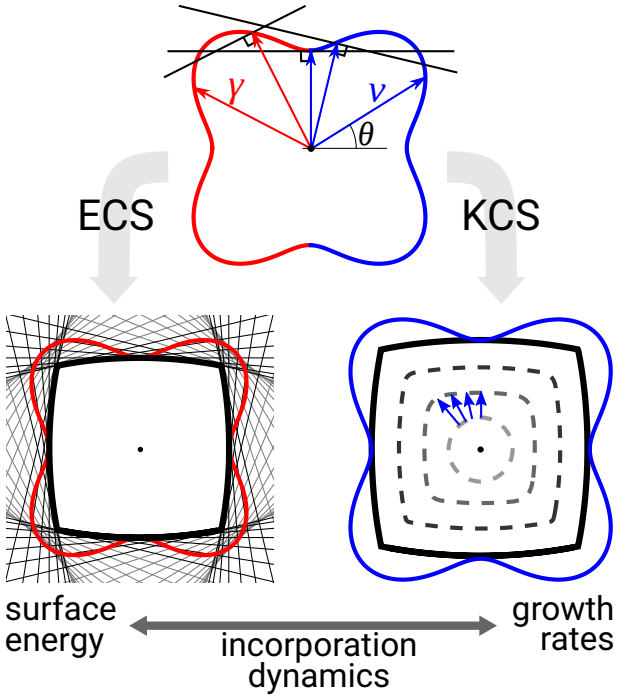

Figure 1 Schematics of the Wulff construction for the ECS, starting from a γ-plot, and the KCS, starting from a v-plot. The geometric construction is the same for both cases and it is sketched for the ECS only. An illustrative growth sequence for the evolution of a circular seed to the KCS is illustrated by the dashed profiles and it is obtained by moving points accordingly.

that can compete, and even overrule, the thermodynamic driving force toward ECS. At the same time, the morphology also diverts from the KCS, making the net growth rate dependent on the adatom flux exchanged between neighboring facets.

In Ref. [13], C. Stöcker and A. Voigt investigated the effect of an isotropic kinetic term on the faceting by annealing of crystal surfaces caused by strongly anisotropic surface free energies. Later, Rätz et al. in Ref [14] introduced an anisotropic kinetic term, depending on the facet orientations. It is the goal of the present work to extend such study to the case of a growing crystal, showing how faceting can change from ECS to KCS by controlling the incorporation kinetics. To this purpose a phase-field (PF) approach [15,16] is exploited, as detailed in the Section 2. Simulation results are first reported for a few test cases in Section 3, showing in a systematic way how the crystal faceting may occur because of anisotropies in the incorporation dynamics. Then, in Section 4, the competition between anisotropic surface energy and/or growth rates and the incorporation dynamics is investigated. More specifically, we show the possibility to account for intermediate morphologies that recover the ECS and the KCS as limiting

cases. Finally, a few applications to morphologies observed in experiments are reported in the Section 5 to validate the method and illustrate its capabilities.

2 Continuum modeling and phase-field approach

Simulations of crystal growth are based on the kinetic model from Ref. [11], exploiting the phase-field approach described in Ref. [14]. Here we briefly review the key concepts of this model and its implementation in the PF framework.

The growth of crystal is typically characterized by a net transfer of matter from a gaseous (or liquid) medium surrounding the crystal into its bulk phase. However, this mechanism proceeds through the crystal surface, where adatoms can move, interact or desorb before being incorporated in a crystal-lattice site [17,18]. The temporal evolution of the adatom density N at a given point $\mathbf{x}$ on the surface can be described by a continuity equation, including an external material supply, i.e. the deposition flux F, and a sink corresponding to the incorporation into the crystalline phase underneath with rate v:

$$\frac{\partial N}{\partial t} = \nabla_\mathrm{s} \cdot [M \nabla_\mathrm{s} \mu] + F - v. \tag{1}$$

M is the adatom mobility, μ is the local adatom chemical potential and ∇_s is the surface gradient operator. The diffusion of adatoms follows the gradient of chemical potential along the surface, $\mathbf{J} = -M\nabla_\mathrm{s}\mu$, according to the Onsager linear law. An additional sink term accounting for the loss of adatoms due to the desorption could be included in the equation but it is here assumed to be negligible. The external flux can in general depend on the facet orientation $F = F(\hat{\mathbf{n}})$. For the sake of simplicity, in the following we shall consider isotropic mobility M.

The attachment/detachment of adatoms into the crystal, resulting in the advancement of the growth front along its normal direction $\hat{\mathbf{n}}$, directly corresponds to the velocity v. In a first approximation, the incorporation rate is proportional to the difference between the chemical potential of an adatom at a location $\mathbf{x}$ on the surface and the chemical potential μ_eq of an atom incorporated within the crystal at the same position:

$$v = (\mu - \mu_\mathrm{eq})/\tau, \tag{2}$$

with τ a kinetic coefficient setting the timescale of the exchange process. More physically, τ corresponds to the adatom lifetime prior to incorporation and is expected to depend on the profile orientation, i.e. $\tau = \tau(\hat{\mathbf{n}})$. By definition, the equilibrium chemical potential is equal to the variation of the system free energy $\mu_\mathrm{eq} = \delta G/\delta N$. As we here just consider surface energy, $\mu_\mathrm{eq} \sim \nabla_\mathrm{s}\xi$, with $\xi = \nabla(r\gamma(\hat{\mathbf{n}}))$ the Cahn-Hoffmann vector (r the magnitude of vector $\mathbf{r} = r\hat{\mathbf{n}}$)[19,20]. In 2D, it can be written in the simplest form $\mu_\mathrm{eq} \sim \kappa(\gamma + \gamma''(\theta))$, with κ the profile curvature, γ the surface energy density and θ the local orientation of the surface.

Following Ref. [11] in the assumption of quasi-stationary conditions for the adatom densities, i.e. $\partial N/\partial t \approx 0$, eqs. 1 and 2 can be combined into a coupled system of equations describing the profile evolution due to adatom incorporation:

$$\begin{cases} v = \nabla_\mathrm{s} \cdot [M \nabla_\mathrm{s} \mu] + F \\ \mu = \mu_\mathrm{eq} + \tau v \end{cases} \tag{3}$$

As stated by the second equation, the adatom chemical potential μ includes both the thermodynamic contribution μ_eq, accounting for the crystal energetics, and a kinetic term, proportional to the profile velocity v. In the limit of infinitely fast incorporation ($\tau \to 0$), the adatom chemical potential reduces to the one of the crystal atoms $\mu \to \mu_{eq}$ and diffusion results only from surface energy differences. In such a case, the evolution will tend to the ECS in the absence of deposition [15,21], or to the KCS if mobility is negligible.

The phase-field approach is well suited to efficiently solve these coupled equations without any geometrical prescription on the crystal shape. Indeed, the profile is traced implicitly by means of the phase-field function φ, set equal to 1 within the crystal and 0 outside, and is nominally located at the $\varphi = 0.5$ iso-surface (or iso-line in 2D), as shown in following plots. In particular, $\varphi(\mathbf{x}) = 0.5[1 - \tanh(3d(\mathbf{x})/\epsilon)]$ with d the signed-distance between the point $\mathbf{x}$ and the surface profile and ϵ a parameter setting the width of the diffused-interface. The motion of the crystal profile is then expressed in terms of the evolution of the φ-field itself, i.e. $v \to \partial\varphi/\partial t$, so that eq. 3 becomes:

$$\begin{cases} \dfrac{\partial \varphi}{\partial t} = \nabla \cdot [M(\varphi)\nabla\mu] + F|\nabla\varphi| \\ g(\varphi)\cdot\mu = \mu_\mathrm{eq} + \tau(\hat{\mathbf{n}})\epsilon\dfrac{\partial\varphi}{\partial t} \end{cases}, \tag{4}$$

where $g(\varphi) = 30\varphi^2(1-\varphi)^2$ is a stabilizing function [22–24] and ϵ is included in the second equation as a scaling factor. $M(\varphi) = M_0(36/\epsilon)\varphi^2(1-\varphi)^2$ is the mobility function restricted to the surface with M_0 an effective coefficient, accounting for the energy barrier for site hopping and following the Arrhenius law.

As detailed in Refs. [15] and [25], the equilibrium chemical potential for the general case of anisotropic γ is

$$\begin{aligned} \mu_\mathrm{eq} = -\epsilon\nabla\cdot[\gamma(\hat{\mathbf{n}})\nabla\varphi] + \frac{1}{\epsilon}\gamma(\hat{\mathbf{n}})B'(\varphi) + \\ -\nabla\cdot\left[\left(-\frac{\epsilon}{2}|\nabla\varphi|^2 + \frac{1}{\epsilon}B(\varphi)\right)\nabla_{\nabla\varphi}\gamma(\hat{\mathbf{n}})\right], \end{aligned} \tag{5}$$

where $\nabla_{\nabla}\varphi$ is the gradient that takes effect along the $\nabla\varphi$ direction. In order to tackle strong anisotropy conditions, the Willmore regularization [15] is implemented, thus introducing a small corner rounding [26]. This adds an additional term to μ_eq in eq. 5:

$$\mu_W = \beta\left[-\nabla^2\omega + \frac{1}{\epsilon^2}B''(\varphi)\omega\right], \tag{6}$$

with $\omega = -\epsilon\nabla^2\varphi + (1/\epsilon)B'(\varphi)$, and β a coefficient to set the strength of the rounding. In particular, the length scale where this term is active is proportional to $\sqrt{\beta}$ [27] and hence it becomes less effective as the particle grows in size. By including this regularization the system of partial differential equations to be solved becomes of sixth order.

In order to set the anisotropic functions $F(\hat{\mathbf{n}})$, $\gamma(\hat{\mathbf{n}})$ and $\tau(\hat{\mathbf{n}})$ in a convenient way, we follow Refs. [21,28], and use the generic continuum function:

$$f(\hat{\mathbf{n}}) = f_0 + \sum_i f_i(\hat{\mathbf{n}} \cdot \hat{\mathbf{m}}_i)^w \cdot \Theta(\hat{\mathbf{n}} \cdot \hat{\mathbf{m}}_i) \qquad (7)$$

with the baseline value f_0 and maxima (or minima if $f_i < 0$) at the assigned orientations $\hat{\mathbf{m}}_\mathbf{i}$, with height (depth) set by f_i and width w. In the following, we set f_0=1 for $F(\hat{\mathbf{n}})$ and $\gamma(\hat{\mathbf{n}})$, while it is 0 for $\tau(\hat{\mathbf{n}})$. w is chosen to exclude any overlap between the different peaks: it is set to 50 for $F(\hat{\mathbf{n}})$ and $\gamma(\hat{\mathbf{n}})$, and to 100 for $\tau(\hat{\mathbf{n}})$. Outward-pointing vectors are only considered thanks to the Heaviside function Θ, thus permitting to treat systems without inversion symmetry and to tune each minimum independently.

Numerical solution of eq. 4 is obtained by Finite Element Methods with the AMDiS toolbox [29,30]. It exploits adaptive mesh refinement allowing for a proper resolution within the diffuse interface region, still guaranteeing a limited computational cost, and a semi-implicit numerical scheme for the temporal integration. For the 2D simulations we set ϵ = 0.05, while for three dimensions (3D) we set ϵ = 0.2.

In the following, we shall use dimensionless parameters for F, γ, τ and M as we here focus on the relative weight of the different contributions in the model without considering any specific material. If experimental time and size scales had to be matched, a unit measure analysis returns the following scaling of the simulation parameters: $[F_0] = [l][t]^{-1}$, $[\gamma_0] = [e][l]^{-2}$, $[\tau_0] = [t][e][l]^{-4}$, $M_0 = [l]^6[e]^{-1}[t]^{-1}$ with respect to the length $[l]$, time $[t]$ and energy $[e]$ units.

3 Faceting by orientation dependent incorporation dynamics. In this section we investigate the formation of faceted crystal shapes during growth as due only to anisotropic incorporation times $\tau(\hat{\mathbf{n}})$. Both isotropic surface energy $\gamma(\hat{\mathbf{n}}) = \gamma_0$ and material supply $F(\hat{\mathbf{n}}) = F_0$ are considered so that the expected ECS and KCS are simply spheres (or circles in 2D).

In Figure 2 the growth sequence of an octahedral particle, starting from a spherical nucleus, is simulated by considering a $\tau(\hat{\mathbf{n}})$ having maxima for all [111] orientations, as shown in the color map in panel (c) for the profile at *t*=2. Because of this choice, the chemical potential of adatoms μ at the center of the $\{111\}$ facets is maximum as they accumulate due to the slow incorporation into the crystal. Conversely, in the regions with intermediate orientations, where adatom incorporation is faster, a lower population and hence a lower μ is obtained. This is made evident in the panel (d) where μ is illustrated by a color map. In particular, the lowest value of μ is found at the facet vertices. Accordingly, a continuous transfer of material occurs by surface diffusion from the facets toward the vertices (and edges), enforcing straight facets. It must be noted that the faceted shape obtained here is not energetically favored and it can be achieved only during growth. Indeed, as shown in panel (e), the energetic contribution to the chemical potential of adatoms μ_{eq} corresponds to the profile curvature since γ is isotropic and would hence drive the system in the opposite direction, toward a global smoothing. While this term is practically ruled-out within the facets, it becomes strong enough at the facet boundaries, causing a local smearing. As evident in the cross-section profiles in Figure 2(b), the rounding is more pronounced at the facet vertices, where the curvature is maximum, while the edges look sharper as forming a wider angle, i.e. lower curvature.

The same principle of transferring material away from the orientation of maximum τ discussed above governs the competing formation and development of different facets. As far as facets have the same τ, they all grow with the same rate, tending to the same polyhedron obtained as KCS by assigning equal F to all facets. However, in the more realistic case where different facets have different ability of incorporating atoms , i.e. different τ, they compete for the incoming material. An example is reported in Figure 3, showing a growth simulation including both $\{111\}$ and $\{110\}$ planes as local maxima in the $\tau(\hat{\mathbf{n}})$ function. In particular, as shown in the color map in the inset, $\tau_{111} < \tau_{110}$. As expected, both facets appear in the growing particle as they tend to slowly incorporate material with respect to the intermediate orientations. Moreover, as $\{110\}$ facets tend to accumulate more adatoms than the $\{111\}$ ones, a net transfer of material from $\{110\}$ to $\{111\}$ facets is observed, frustrating the lateral expansion of the $\{111\}$ facets in advantage of the $\{110\}$ ones. This is demonstrated by the μ color map, maximum on $\{110\}$ facets and slightly lower on the $\{111\}$ ones. Figure 3 also reports a view of μ_{eq} having high values at the facet edges and vertices due to high curvatures, showing thus that the observed faceting is in contrast with the surface energetics.

The magnitude of material transfer between the facets directly depends on their difference in incorporation times, i.e. on their relative population of adatoms. This is made evident in Figure 4 where the faceted growth of an initially circular 2D profile, determined by considering local maxima of τ in both $\{10\}$ and $\{11\}$ directions, is compared for a case where τ_{10} is just a 10% greater than τ_{11} and another where it is twice larger. In the former case, both $\{10\}$ and $\{11\}$ facets coexist, returning an octagonal shape with $\{10\}$ segments extending slightly more than $\{11\}$ ones. In the latter case, on the contrary, the actual growth rate of $\{11\}$ facets is dramatically enhanced by the adatom diffusion from the slow $\{10\}$ so that it shrinks in size up to disappear from the crystal shape, leaving a $\{10\}$-bounded square.

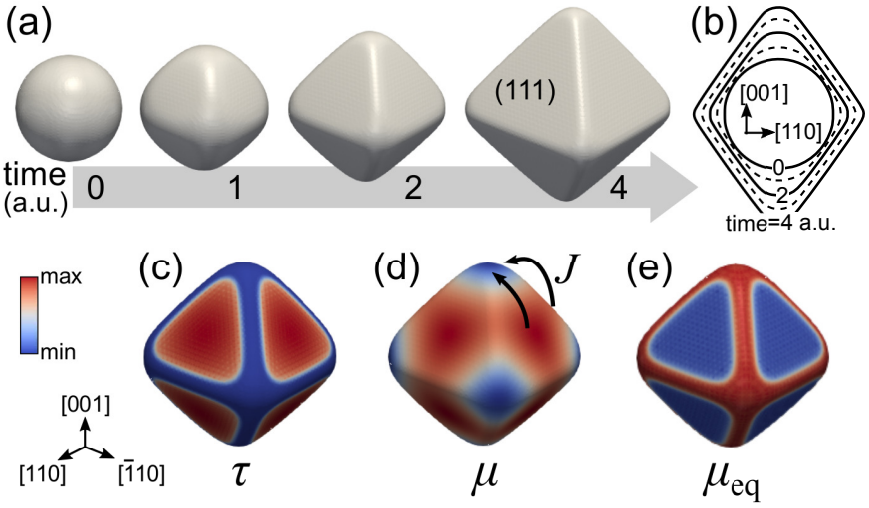

Figure 2 (a) Growth simulation of a $\{111\}$ faceted shape with the kinetic incorporation term. (b) Time evolution of cross-section profiles. Color map for (c) the incorporation time τ, (d) the chemical potential μ and (e) the equilibrium chemical potential $\mu_{\rm eq}$, corresponding to the surface curvature. τ_{111} = 20 and M_0 = 0.1 .

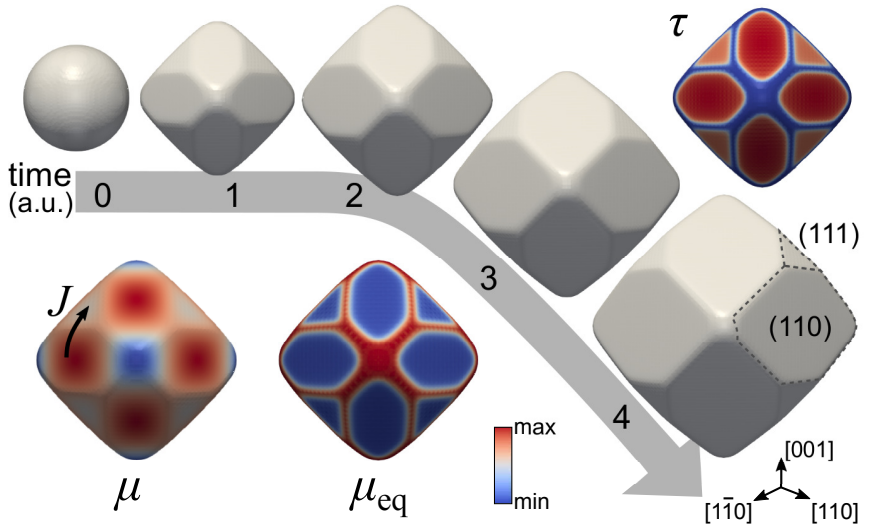

Figure 3 Growth simulation of a faceted shape with competing $\{110\}$ and $\{111\}$ facets, with τ = 20 and 16 respectively. Color maps show the the incorporation time τ, the chemical potential μ and the equilibrium chemical potential $\mu_{\rm eq}$ on the surface. M_0 = 0.1 .

As the faceting behavior due to the incorporation kinetics has been so far discussed in terms of dominance of the slowest growing facets, it closely relates with the principles of the KCS. Indeed, the hierarchy of incorporation times roughly corresponds to the hierarchy of the facet growth rates. However, at variance with the KCS construction, facet velocities are not assigned constants but are dynamically determined by the redistribution of adatoms between the competing facets. This process is enabled by the surface diffusion and it is then effective only over a distance within the actual diffusion length. The finite extent of the diffusion length has a great impact on the faceting evolution, as made evident in the Figure 5 where the effect of changing the particle size or the surface mobility on the $\{10\}$ vs. $\{11\}$ facets is shown for two ratios of incorporation times. Panels (a) and (b) illustrate the evolution sequence for two τ ratios, starting from an initial circle of small size. As already discussed, the facets with higher τ, here the $\{10\}$, are going to prevail in the growing shape. In (a), the transfer of material toward $\{11\}$ facets is larger so that they shrink and quickly disappear, leaving a square shape. In (b), the transfer of material is lower as the incorporation on the two facets is more similar, so that $\{11\}$ facets persist for a longer time. To better compare the different timescale in the two cases, the ratio of the length of $\{10\}$ vs. $\{11\}$ segments is plotted against the evolution time in Figure 5(c). In both cases, the shrinkage of $\{11\}$ facets is exponential, with a lower velocity for the smaller τ ratio. Indeed, as the facet size decreases, the same amount of material coming from the $\{10\}$ facets is spread over a shorter length and hence result in an increment of the growth rate.

By repeating the evolution starting from a particle with a four-times larger diameter, the $\{10\}/\{11\}$ ratio grows significantly slower for both cases since the diffusion cannot cover the whole facet size, thus making the facet com-

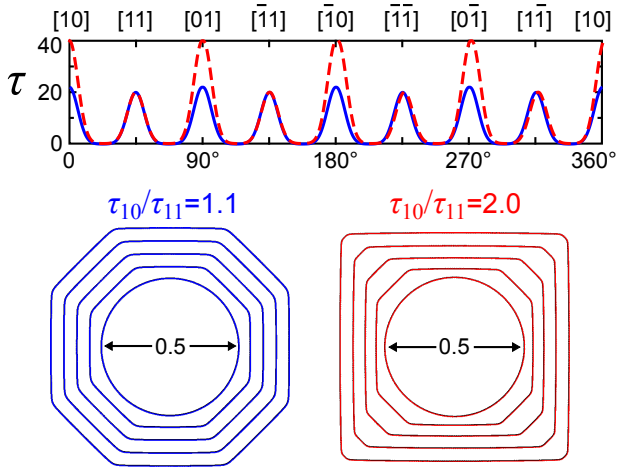

Figure 4 Comparison of the shape evolution from circular to faceted shape for different τ_{10}/τ_{11} ratios, by using the anisotropy functions shown in the top panel.

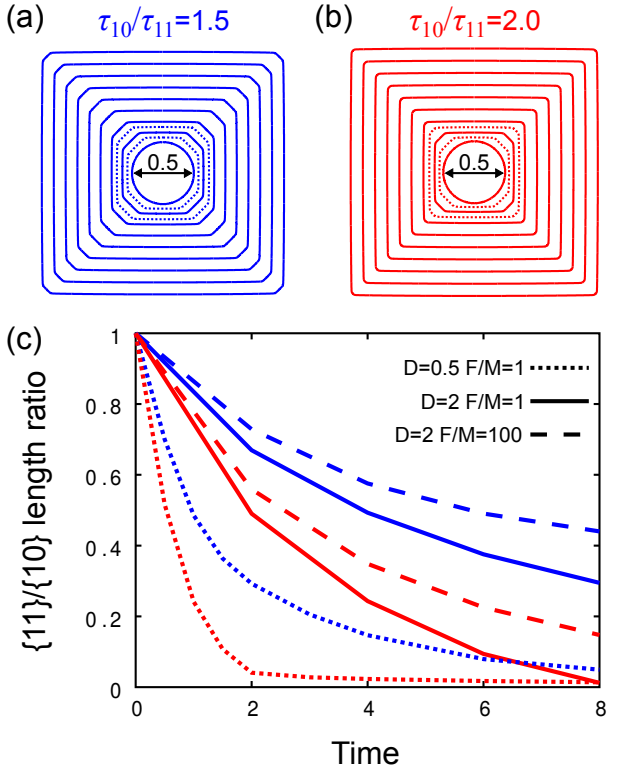

Figure 5 (a-b) Time evolution of the surface contours for two different τ_{10}/τ_{11} ratios. (c) Plot of the $\{10\}/\{11\}$ area ratio for two sets of τ (blue as in panel (a), red as in panel (b)) for different diameters D of the initial shape and F_0/M_0 ratios.

petition less effective. It is then worth mentioning that this size dependency makes an important difference with respect to the kinetic Wulff construction, which on the contrary always returns a self-similar morphology. A similar effect can be achieved by decreasing the surface mobility as reported by the shallowest curves in the plot. Even if material always tends to flow from the facets with slower incorporation with respect to the neighboring ones, the timescale for this process can become slow enough to consider the multifaceted morphology as metastable.

4 Competing regimes driving the crystal faceting

The faceting induced by orientation-dependent incorporation times requires surface diffusion to be established. Moreover, in order to enforce the faceting by τ-anisotropy, the kinetic term entering μ must be larger than $\mu_{\rm eq}$ (see eq. 3). This competition is made evident in Figure 6, where simulation profiles obtained for different incorporation times (a) and deposition fluxes (b) are compared at the same growth stage. Longer incorporation times τ and larger material supply by means of larger F values, enforce the kinetic regime. In the opposite case, $\mu_{\rm eq}$ prevails in driving the diffusion toward a rounded shape, corresponding to the ECS since γ is isotropic. More precisely, the balance between the kinetic and energetic contribution is given by the ratio $\mu_{\rm eq}/(\tau v) = (\kappa\gamma)/(\tau v)$ and hence it also depends on the actual profile, as due to the local curvature κ. Indeed, high curvature regions will be strongly contrasted by surface energy, thus resulting in smoothed profiles even if a kinetic faceting is achieved elsewhere. This can be observed in the intermediate profile of Figure 6(a) where a faceted squared-shape is obtained except for a local rounding at the vertices. More generally, as sharp vertices correspond to singularities in the local curvature, they will always tend to smooth, on a local scale as small as the τv term dominates. Also, as for a circle the curvature directly relates to its radius $\kappa = 1/R$, the strength of $\mu_{\rm eq}$ will progressively decrease as the growth proceed so that those rounded profiles in Figure 6 will eventually tend to facets when their radius becomes large enough.

A similar competition can be illustrated for the more realistic case of anisotropic surface energy. In such a case, if the τ maxima coincide with the γ minima, both incorporation kinetics and surface energy will enforce the same faceting, eventually accelerating the shape transformation. Viceversa, if the set of expected facets for τ and γ differs, the resulting shape will depend on their relative strength. As an example, in Figure 7 we consider a $\gamma = \gamma(\hat{\mathbf{n}})$ with deep minima along $<10>$ directions dominating the ECS, while τ has maxima in the $<11>$ directions, where γ has only shallow minima (panel a). If the τ/γ is small enough (panel b), the main driving force causing the redistribution of the (isotropically) deposited material is the energy minimization, so that the profile tends to the ECS exposing the most stable $\{10\}$ facets despite their fast incorpo-

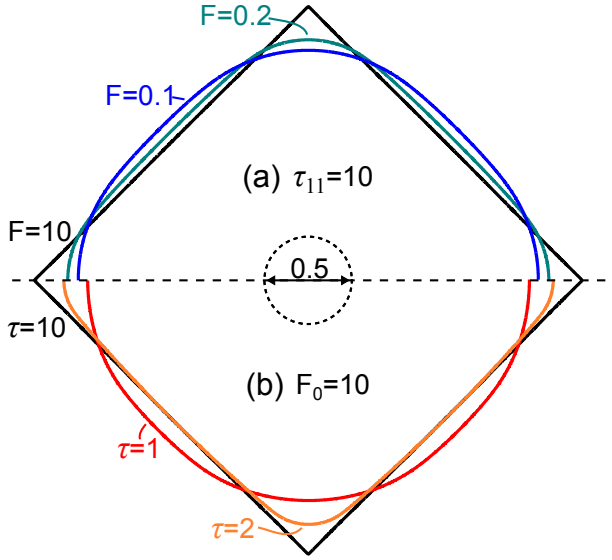

Figure 6 Comparison of the out-of-equilibrium conditions needed for the kinetic faceting. (a) Profiles obtained by changing the deposition flux, for a fixed τ_{11} = 10. (b) Profiles obtained by changing τ_{11}, for the same F_0 = 10. All the profiles have the same volume, and the initial stage is a circle. M_0 = 0.1 .

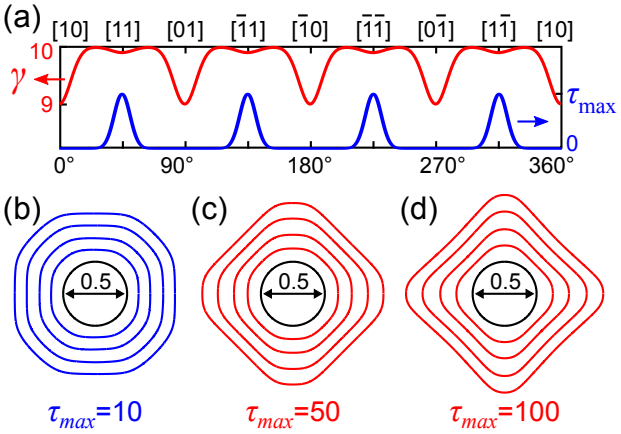

Figure 7 Competing role of incorporation time and surface energy anisotropy. For larger τ (center and right) the kinetic faceting dominates over the thermodynamic one resembling the ECS (left). Corner regularization is used with β = 0.05, while the anisotropy functions for $\tau(\hat{\mathbf{n}})$ and $\gamma(\hat{\mathbf{n}})$ are plotted in the top panel.

ration rate. Viceversa, when increasing the τ/γ ratio, the role of the different kinetics becomes dominant, hindering the growth of the most stable $\{10\}$ facets in favor of the slower growing $\{11\}$ facets. Then, a rotated $\{11\}$-faceted squared profile tends to form (panel c and d), even if a much higher energy compared to the ECS is retained. Evidently, if the growth would be interrupted, the following evolution would drive the system toward the ECS, eventually following a kinetic path influenced by the anisotropic τ.

The distribution of material supply can be anisotropic as well, $F = F(\hat{\mathbf{n}})$, driving the system toward the KCS, and then compete with the anisotropic incorporation times in determining the crystal morphology, as illustrated in Fig. 8. If maxima in τ coincide with minima of F, both terms will lead to the same faceting, as in the case of the panel (b). On the contrary, if τ-maxima and F-minima do not correspond, as in panels (c) and (d) where they are out-of-phase by 45°, the actual faceting results from the competition between them. In particular, since the faceting due to $\tau(\hat{\mathbf{n}})$ requires diffusion, it is expected to prevail only in the case of a smaller F/M ratio and only if the size does not exceed the actual diffusion length. These conditions are not fulfilled in the case in panel (c), where the diffusion is frustrated by the fast growth rate, so that the faceting is given by the minima in F, as for the KCS. A small trace of diffusion from the $\{11\}$ vertices to the $\{10\}$ facets is barely distinguishable and too weak for altering the shape evolution. On the contrary, by reducing the F/M ratio it is possible to significantly enhance the transfer of the deposited material prior to the incorporation into the crystal so that the shape evolution depends more on the different τ. This is the case for the first evolution stages in the Figure 8(d), where the $\{11\}$ facets, corresponding to τ maxima, are clearly recognizable despite corresponding to the F maxima. However, the extent of material transfers is limited by the diffusion length while the profile size becomes indefinitely large as the growth proceeds. Therefore, at some point, the faceting sustained by diffusion is out-ruled by the anisotropy of the growth rates F and the shape tends to the expected KCS as evident in the latest stages of the reported evolution. Notice that a certain broadening due to local diffusion is always present at the $\{11\}$ corners, trying to preserve the slow incorporating facets. However, it remains limited in a region as long as the diffusion length and hence it becomes negligible for a very large diameter. This example allows us to conclude that the faceting induced by orientation-dependent incorporation times τ plays a major role for particle sizes as small as the diffusion length while it loses efficacy for larger sizes where the system tends to the KCS determined by the anisotropy in the growth rates F.

Finally, it is worth noting that the balance between the different contributions driving the faceting holds on a local scale so that, the same growing system may behave differently from one region to the other. This is not unusual if one considers directional deposition [31,32] or shielding effects [18,33] with material arriving only on a certain portion of a sample and possibly diffusing on other regions. To illustrate this situation, in Figure 8(e) the evolution of an initially circular profile with material supply only from the right-hand side is considered. As expected the growth

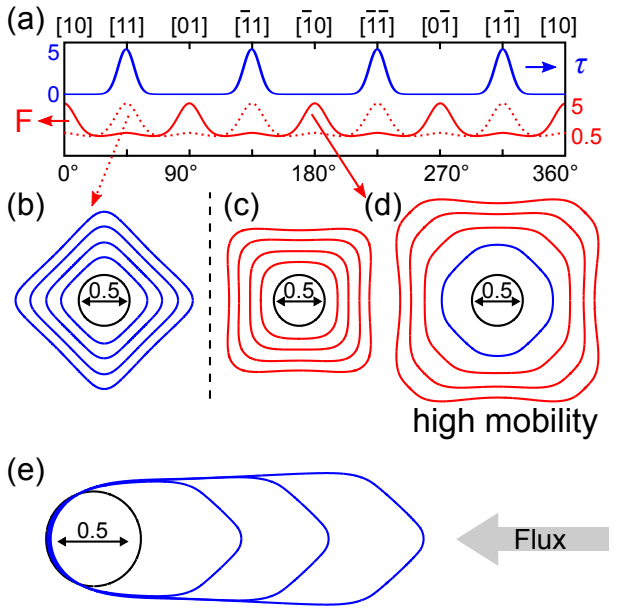

Figure 8 Combination of anisotropic incorporation time and material supply. (a) Plot of the $F(\hat{\mathbf{n}})$ and $\tau(\hat{\mathbf{n}})$ anisotropy functions used. (b) Both anisotropies lead to the $\{11\}$ square (M_0=0.001). (c) The flux anisotropy is rotated by 45° (dotted line in panel (a)) and imposes $\{10\}$ faceting (M_0=0.001). (d): the mobility is increased (M_0=0.007), while keeping the opposite anisotropies for flux and kinetics as in (c). (e) The flux F_0 = 5 is directed on one side of the crystal, following the arrow.

proceeds asymmetrically, with material accumulation on this latter side. Kinetic faceting is obtained there as the deposited material is redistributed according to the different incorporation times. On the opposite side, a small amount of material diffuses by surface diffusion under the influence of the thermodynamic driving force thus favoring a rounded profile of larger radius, due to the isotropic γ. Then, on the same particle a faceted growing region, controlled by the incorporation times τ, and a smooth circular one, driven by the energy reduction, coexist.

5 Applications to realistic structures As observed in the previous section, the kinetically faceted shapes exist only in connection with growth and do not necessarily correspond to the most stable morphologies. Post-growth, high-temperature processes, e.g. annealing, could drive further changes in the crystal shape, still influenced by the incorporation kinetics (see [13]), but directed toward the ECS. Nonetheless, kinetic faceting is fully meaningful in experiments when growth is the only high temperature process at which surface diffusion is active. The model discussed here finds a direct application to several different experimental systems where out-of-equilibrium growth conditions return peculiar faceting different from both the ECS and the KCS. To validate this, here we show a couple of examples where taking into account the incorporation dynamics is essential to capture the details of the growth mechanism.

In Figure 9 we simulate the growth of a faceted crystal starting from a simple parallelepiped, laterally bounded by $\{110\}$ planes and terminated by a (001) top facet. Incorporation times are assumed to be maximum for these facets and for $\{111\}$ planes, with τ_{001} one order of magnitude smaller. A vertical deposition flux oriented along the [00-1] direction is considered. The growth sequence for a small base structure is reported in panel (a). Since the early stages, $\{111\}$ facets nucleate and tend to grow larger at the expenses of the (001) top, up to form a pyramidal tip. This process results from a continuum transfer of material from the slow incorporating $\{111\}$ facets to the faster (001), resulting in a significant enhancement of its growth rate. The process is not linear in time as it would be expected by simply assigning different facet velocities as in a KCS construction, but proceeds exponentially. Indeed, the larger the $\{111\}$ grows the more material is driven by diffusion to the (001), whose area is continuously shrinking at a faster pace. In panel (b), an intermediate profile obtained for the same conditions but considering a larger base width is shown and compared with a case obtained for lower mobility (panel c). Reasonably, the larger dimensions lead to a delay of the closure of the $\{111\}$ pyramid, requiring a greater amount of material to diffuse onto the (001) top. Furthermore, the selected size is large enough to exceed the diffusion length and hence, the material moved from the $\{111\}$ facets to the borders of the (001) top cannot spread uniformly on it, as in the case of panel (a), thus producing overgrowth mounds along the (001) perimeter. These are better noticeable in the plot in panel (d) where the profile is traced in cross-section along the [110] direction. Evidently, the lateral extension of the mounds directly depends on the actual diffusion length as the peaks are much broader and shallower in the high mobility case. These simulations closely compare with the experiments of micro-crystals growth on pillar-patterned substrates reported in Refs.[18, 34–36]. Indeed, therein the growth conditions were pushed toward a kinetic regime by exploiting a Low-Energy Plasma-Enhanced Chemical Vapour Deposition, allowing for the deposition of several μm of Ge by high growth rates (4-7.5 nm s^{-1}) at relatively low temperatures (400-600 °C). Our results offer a deeper insight on the possible mechanisms responsible for the observed temperature dependence of the crystal morphology, changing from nearly planar at low temperature to pyramidal at higher temperature. Indeed, according to the simulations, the pyramidal shape is achieved only if diffusion is active, which is the case of high enough temperature. The consistency of the simulation results with the experimental evidences is also corroborated by the overgrowth features recognized on larger structures. A more quantitative anal-

ysis, aimed at the determination of the characteristic facet incorporation times, is left to a future, more focused work.

In a recent study [37], the growth by Selective-Area Epitaxy of GaAs nanomembranes [38] has been demonstrated to proceed in a kinetic regime dominated by the large difference in the adatom incorporation times of the exposed facets. In particular, by performing a Molecular Beam Epitaxy growth (with 1 $\text{Å}s^{-1}$ deposition rate for 60 min.), μm-long trapezoidal fins bounded by $\{110\}$ facets and a (111)B at the top were observed to evolve toward a triangular shape, with a progressive shrinkage of the (111)B facet. This mechanism was explained by considering that incorporation of the top facet is faster than on $\{110\}$ ones and a difference of an order of magnitude was estimated between the respective incorporation times: $\tau_{110} \approx 10\tau_{111}$. In Figure 10 we show a comparison of growth simulations of a fin-like structure by taking into account both orientation dependent incorporation times and anisotropic surface energy (neglected in Ref. [37]). In particular, the sequence in panel (a) is obtained by considering just anisotropic surface energy $\gamma(\hat{\mathbf{n}})$, compatible with literature values from Ref. [39]. This is compared with the sequence in panel (b), achieved when admitting also the expected differences in the incorporation times. Evidently, in the former case the criterion of free-energy minimization causes a strong redistribution of material into a compact shape, faceted according to the relative stability of the considered facets. Indeed, at the latest stages of the evolution, the growing crystal closely resemble the ECS, except for the bottom portion within the slit that is distorted by the non-contact boundary condition imposed at the sides of the slit to mimic the effect of the oxide mask. Viceversa, in the case of panel (b), the thermodynamic driving forces are cancelled by the strong difference in incorporation times. Thus, the morphology evolves in a kinetic regime where $\{110\}$ facets extend from the slit perimeter returning a shape evolution very similar to the experimental one. It is worth noting how in this example both γ and τ anisotropies are considered as expected for the real system thus showing how the latter plays a major role at the experimental conditions, still maintaining the energy differences between the facets. If, after growth, the fins were annealed at high temperature, material would possibly evolve to restore the most convenient facets more similar to the case of panel (a).

6 Conclusions The role of orientation-dependent incorporation kinetics in driving the faceting of a crystal has been in-depth analyzed by means of growth simulations. It has been shown that large differences in the incorporation times can play a major role in the faceting of a crystal during growth, and compete with the anisotropies in surface energy and material supply. The interplay of all of these factors has been discussed in details and it is shown to allow for crystal shapes beyond the simplistic description of ECS and KCS. This makes the approach well suitable to tackle realistic cases.

It must be however noted that, as for the growth rates in the KCS, also the incorporation times τ are not simple to be estimated a-priori as this would require an extensive and dedicated analysis of the atomistic processes behind adsorption and redistribution of atoms within the surface of a crystal under out-of-equilibrium growth conditions. Nonetheless, at variance with the growth velocities, incorporation times are expected to be independent of the growth parameters and hence to be real properties of the material.

Acknowledgements We acknowledge financial support from the European Union through Horizon-2020 FET μ-SPIRE Project No. 766955. M.S acknowledges the support of the Postdoctoral Research Fellowship awarded by the Alexander von Humboldt Foundation (Germany). We acknowledge the CINECA award under the ISCRA initiative, for the availability of high performance computing resources and support, and the computational resources from the Center for Information Services and High Performance Computing (ZIH) at TU-Dresden and Jülich Supercomputing Center within Project No. HDR06.

References

[1] L. D. Marks and L. Peng, J. Phys. Condens. Matter **28**(5), 053001 (2016).
[2] G. Wulff, Zeitschrift fur Kryst. und Mineral. **34**(5/6), 449–530 (1901).
[3] C. Herring, Angewandte Chemie **65**(1), 34–35.
[4] J. E. Taylor, JOM **48**(12), 19–22 (1996).
[5] W. C. Carter, J. E. Taylor, and J. W. Cahn, JOM **49**(12), 30–36 (1997).
[6] F. C. Frank, On the Kinematic Theory of Crystal Growth and Dissolution Processes (John Wiley & Sons, New York, 1958).
[7] A. A. Chernov, Soviet Physics Crystallography **7**, 728–730 (1963).
[8] J. W. Cahn and W. C. Carter, Metall. Mater. Trans. A **27A**, 1431–1440 (1996).
[9] S. H. Jones, L. K. Siedel, and K. M. Lau, J. Cryst. Growth **108**, 73–88 (1991).
[10] Slow growing facets are the one prevailing in a convex region, as is the growing shape of a regular crystal. On the contrary, concave regions result in the enlargement of fast growing facets.
[11] J. W. Cahn and J. E. Taylor, Acta Metall. Mater. **42**(4), 1045–1063 (1994).
[12] E. Fried and M. E. Gurtin, Adv. Appl. Mech. **40**(04), 1–177 (2004).
[13] C. Stöcker and A. Voigt, J. Cryst. Growth **303**(1), 90–94 (2007).
[14] A. Rätz, A. Ribalta, and A. Voigt, J. Comput. Phys. **214**(1), 187–208 (2006).
[15] B. Li, J. Lowengrub, A. Rätz, and A. Voigt, Commun. Comput. Phys. **6**(3), 433–482 (2009).
[16] R. Bergamaschini, M. Salvalaglio, R. Backofen, A. Voigt, and F. Montalenti, Advances in Physics: X **1**(3), 331–367 (2016).

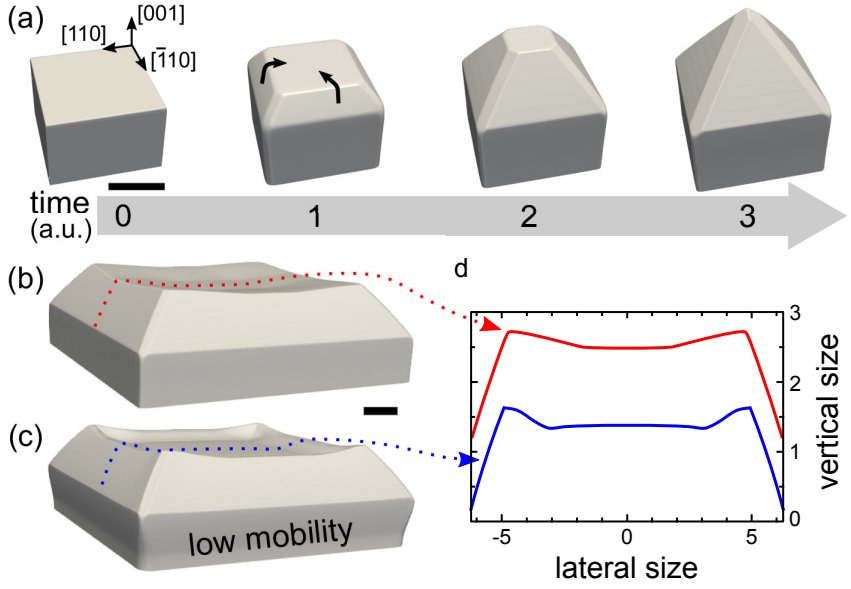

Figure 9 (a) Time evolution of a pillar top with competing incorporation times for the top (001) and the lateral $\{111\}$ and $\{110\}$. (b-c) Comparison of the growth on a 4-times larger base for two different mobility coefficients ((c) 10 times smaller). (d) Comparison of the central (110) cross-sectional profiles, shifted arbitrarily in the vertical direction. The flux $F_0 = 0.5$ is vertical, $\tau_{110} = \tau_{111} = 10$, $\tau_{001} = 1$. The scale bar is 1.5 length units.

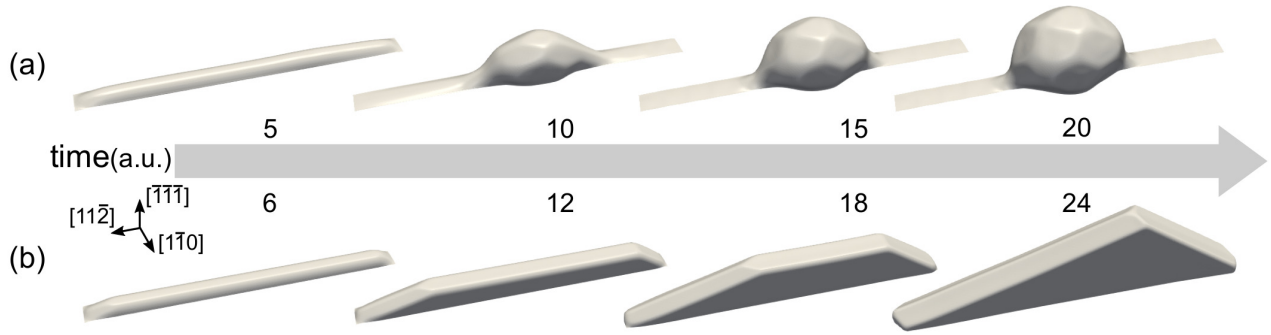

Figure 10 Selective-area growth of GaAs crystal in a pure thermodynamic regime (a) and in a kinetic regime (b) with $\tau_{110} = 100$ and $\tau_{111} = 10$. The surface energy is anisotropic with $\gamma_{111B} = 0.89$, $\gamma_{111A} = 0.99$, $\gamma_{110} = 0.90$, $\gamma_{100} = 0.90$. Corner regularization is used with $\beta = 0.001$. Material is deposited with a flux distribution at a 45° angle.

[17] M. Ohtsuka and A. Suzuki, J. Appl. Phys. **73**(11), 7358–7369 (1993).

[18] R. Bergamaschini, F. Isa, C. Falub, P. Niedermann, E. Müller, G. Isella, H. von Känel, and L. Miglio, Surf. Sci. Rep. **68**(3-4), 390–417 (2013).

[19] D. W. Hoffman and J. W. Cahn, Surf. Sci. **31**(1972), 368–388 (1972).

[20] J. W. Cahn and D. W. Hoffman, Acta Metall. **22**, 1205–1274 (1974).

[21] M. Salvalaglio, R. Backofen, R. Bergamaschini, F. Montalenti, and A. Voigt, Cryst. Growth Des. **15**, 2787–2794 (2015).

[22] C. Gugenberger, R. Spatschek, and K. Kassner, Phys. Rev. E **78**(1), 16703 (2008).

[23] A. Voigt, Appl. Phys. Lett. **108**(3), 036101 (2016).

[24] R. Backofen, S. Wise, M. Salvalaglio, and A. Voigt, International Journal of Numerical Analysis and Modeling pp. In press, arXiv:1710.09675.

[25] S. Torabi, J. Lowengrub, A. Voigt, and S. Wise, Proc. R. Soc. A **465**(2105), 1337–1359 (2009).

[26] B. J. Spencer, Phys. Rev. E **69**, 11603 (2004).

[27] T. Philippe, H. Henry, and M. Plapp, Journal of Crystal Growth **503**(June), 20–27 (2018).

[28] M. Salvalaglio, R. Bergamaschini, R. Backofen, A. Voigt, F. Montalenti, and L. Miglio, Applied Surface Science **391**, 33–38 (2017).

[29] S. Vey and A. Voigt, Comput. Vis. Sci. **10**(1), 57–67 (2007).

[30] T. Witkowski, S. Ling, S. Praetorius, and A. Voigt, Adv. Comput. Math. **41**, 1145 (2015).

[31] M. M. Hawkeye and M. J. Brett, Journal of Vacuum Science & Technology A **25**(5), 1317–1335 (2007).

[32] A. Barranco, A. Borras, A. R. Gonzalez-Elipe, and A. Palmero, Progress in Materials Science **76**, 59 – 153 (2016).

[33] M. Salvalaglio, R. Backofen, and A. Voigt, Physical Review B **94**(23), 235432 (2016).

[34] C. V. Falub, T. Kreiliger, F. Isa, A. G. Taboada, F. Pezzoli, R. Bergamaschini, A. Marzegalli, D. Chrastina, G. Isella, A. Neels, P. Niedermann, A. Dommann, and L. Miglio, Thin Solid Films **557**, 42–49 (2014).
[35] A. Taboada, M. Meduna, M. Salvalaglio, F. Isa, T. Kreiliger, C. Falub, E. Barthazy Meier, E. M?ller, L. Miglio, G. Isella, and H. Von Känel, Journal of Applied Physics **119**(5) (2016).
[36] R. Bergamaschini, S. Bietti, A. Castellano, C. Frigeri, C. V. Falub, A. Scaccabarozzi, M. Bollani, H. von Känel, L. Miglio, and S. Sanguinetti, J. Appl. Phys. **120**(24), 245702 (2016).
[37] M. Albani, L. Ghisalberti, R. Bergamaschini, M. Friedl, M. Salvalaglio, A. Voigt, F. Montalenti, G. Tütüncüoglu, A. Fontcuberta i Morral, and L. Miglio, Phys. Rev. Mater. **2**(9), 093404 (2018).
[38] G. Tutuncuoglu, M. De la Mata, D. Deiana, H. Potts, F. Matteini, J. Arbiol, and A. Fontcuberta i Morral, Nanoscale **7**(46), 19453–19460 (2015).
[39] N. Moll, A. Kley, E. Pehlke, and M. Scheffler, Phys. Rev. B **54**(Sep), 8844–8855 (1996).